Influence of laser intensities on the dissociation of hydrogen molecular ions

Tian-Yu Xu and Feng He*

Key Laboratory for Laser Plasmas (Ministry of Education) and Department of Physics and Astronomy, Shanghai Jiao Tong University, Shanghai 200240, People's Republic of China

(Received 29 July 2014; published 3 November 2014)

We systematically study the influence of laser intensities on the dissociation of H_2^+ in strong laser fields by numerically solving the time-dependent Schrödinger equation. In Ti:sapphire infrared (IR) laser fields, H_2^+ mainly dissociates along $1s\sigma_g$ and $2p\sigma_u$ states. The mixture of these dissociative states results in the laser-intensity-dependent electron asymmetric localization. When the dissociation process is dressed by a laser field with a very long wavelength, the potential surfaces $1s\sigma_g$ and $2p\sigma_u$ degenerate due to the Stark effect, hence the kinetic energy release is changed. When H_2^+ is exposed to a strong ultraviolet (UV) pulse, H_2^+ is pumped to several excited states by absorbing a few energetic photons, resulting in the molecular dissociation ending with several kinetic energy peaks. The discrepancy of simulation results from the numerical models with and without Born-Oppenheimer approximation are analyzed.

DOI: 10.1103/PhysRevA.90.053401 PACS number(s): 33.80.Rv, 33.80.Wz, 42.50.Hz, 42.65.Re

I. INTRODUCTION

When a molecule is exposed to strong laser fields, one of the chemical reaction pathways is that the molecule absorbs one or several photons and is excited from the bound ground state to repulsive excited states, followed by molecular dissociation. In this process, the molecular potential energy is finally converted into the kinetic energy release (KER) of fragments [1]. In past decades, the control of dissociation pathways and KER has attracted a lot of attention. As the simplest molecule, H_2^+ works as a prototype and has been studied extensively [2]. Several dissociation mechanics have been discovered, such as bond softening[3,4], bond hardening [5], above-threshold dissociation [6], and tunneling dissociation [7]. By controlling the absorbed photons, H_2^+ may dissociate through selected potential surfaces with electronic states having the same or opposite parities. The interference of such dissociation pathways may cause asymmetric electron localization on two nuclei after the dissociation. A series of strategies has been applied to control the asymmetric electron localization, such as two-color fields [6,8–10], single phase stabilized few-cycle Ti:sapphire pulse [11–17], UV-pump–IR-probe [18–20], attosecond pulse train plus IR fields [21,22], IR-pump–IR-probe [23–26], or even with a single symmetric laser pulse [27].

Besides the most popular dissociation channels, i.e., $1s\sigma_g$ and $2p\sigma_u$, H_2^+ may also dissociate along π orbitals if it is pumped by a UV pulse whose polarization axis is perpendicular to the molecular axis [28]. Recently, Fischer *et al.* [29] reported that the dissociative double excited H_2 may decay into a free electron and H_2^+ dissociating along either $1s\sigma_g$ or $2p\sigma_u$.

The molecular dissociation has been controlled by carrier envelope phases, wavelengths, pulse durations, and time delays between pulses [30–33]. In this paper, we systematically study laser intensity effects on the dissociation of H_2^+ [34–39]. Depending on laser intensities and photon energies, H_2^+ may dissociate along selected electronic potential curves, and the dissociative fragments gain different kinetic energies. The rest of the paper is organized as follows. In Sec. II, we study the dissociation of H_2^+ in Ti:sapphire laser pulses with different intensities. The Stark effect on dissociation is presented in Sec. III. In Sec. IV, the molecular dissociation along some higher electronic states by absorbing multiple high energetic photons are discussed. The paper ends with a conclusion in Sec. V.

II. DISSOCIATION OF H_2^+ in Ti:SAPPHIRE LASER PULSES

A. Numerical model

In this section, we study the dissociation of H_2^+ in the UV-pump–IR-probe interaction strategy. The relatively weak time-preceding attosecond UV pulse resonantly excites H_2^+ from $1s\sigma_g$ to $2p\sigma_u$, and the following dissociation is manipulated by the time-delayed Ti:sapphire laser pulse. The polarization axes of both pulses are parallel to the molecular axis. The whole interaction only keeps tens of femtoseconds, hence the molecular rotation has been neglected. Since the potential surfaces $1s\sigma_g$ and $2p\sigma_u$ are far away from other electronic states, we only include these two lowest electronic states considering the fact that the UV pulse is weak and the IR photon energy is very small. Within the Born-Oppenheimer approximation (BOA), the wave function of H_2^+ in terms of the two lowest-lying electronic states can be expressed as

$$\Phi(\vec{r},R,t) = \chi_g(R,t)\phi_g(\vec{r},R) + \chi_u(R,t)\phi_u(\vec{r},R), \quad (1)$$

where $\vec{r}$ is the three-dimensional coordinates of the electron, R is the internuclear distance, ϕ_g and ϕ_u represent the electronic $1s\sigma_g$ and $2p\sigma_u$ states, respectively, and χ_g and χ_u are the corresponding nuclear wave packets (NWP). Insertion of Eq. (1) into the time-dependent Schrödinger equation (TDSE) yields the following two-channel equation [40] (atomic units are used unless stated otherwise)

$$i\frac{\partial}{\partial t}\begin{pmatrix}\chi_g(R,t)\\ \chi_u(R,t)\end{pmatrix} = \begin{pmatrix}T_R+V_g & V_{gu}\\ V_{gu} & T_R+V_u\end{pmatrix}\begin{pmatrix}\chi_g(R,t)\\ \chi_u(R,t)\end{pmatrix}, \quad (2)$$

where $T_R = -\frac{1}{M}\frac{\partial^2}{\partial R^2}$ with M being the nucleus mass, and V_g and V_u are the electronic potential energies, V_{gu} is the dipole coupling between $1s\sigma_g$ and $2p\sigma_u$.

*fhe@sjtu.edu.cn

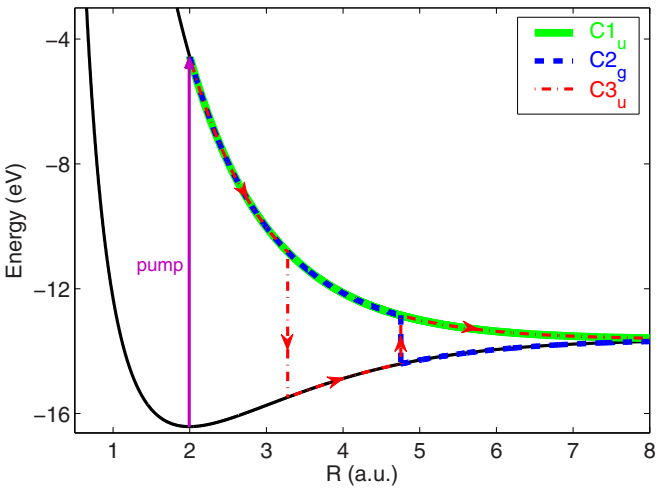

FIG. 1. (Color online) Potential curves for H_2^+ in two lowest electronic states. The UV pump pulse resonantly excites H_2^+ from $1s\sigma_g$ to $2p\sigma_u$, followed by the dissociation controlled by the time-delayed IR laser pulse. Several possible dissociation pathways are sketched.

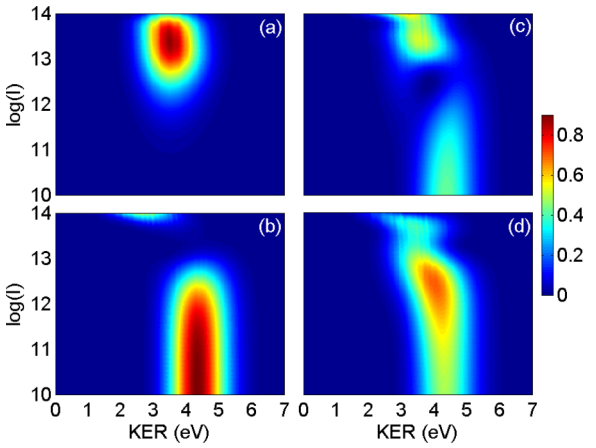

FIG. 2. (Color online) Intensity-dependent KER distribution for H_2^+ dissociating along (a) $1s\sigma_g$, (b) $2p\sigma_u$, or the states that the electron locates on (c) the left nucleus and (d) the right nucleus. The time delay is fixed at $\tau = -1.2T_{800}$, the carrier envelope phase $\theta = 0$. The base of the logarithm in the whole paper is 10.

The combined pump-probe electric field is written as

$$E = E_{\rm UV}\sin(\omega_{\rm UV}t)\exp[-4\ln 2(t/\tau_{\rm UV})^2] + E_{\rm IR}\cos[\omega_{\rm IR}(t+\tau)+\theta]f(t+\tau), \quad (3)$$

where τ is the time delay, and θ is the carrier envelope phase. The time-delayed IR pulse has a trapezoidal envelope $f(t)$ with a six-cycle plateau and one-cycle turn on and one-cycle turn off. Note that the numerical results from the trapezoidal and Gaussian laser pulses are similar, while the former offers a relatively long plateau with a constant intensity. The UV pulse has the intensity 10^{13} W/cm^2 and wavelength 106 nm. The corresponding UV photon energy matches the energy gap between $1s\sigma_g$ and $2p\sigma_u$ at the equilibrium internuclear distance. The spatial grid covers the range $R = 0$ to 200 a.u. and $\Delta R = 0.04$ a.u. The time step $\Delta t = 1$ a.u. We use the split-operator method to propagate Eq. (2) [41]. We keep propagating the wave packet until the dissociative part enters the area $R > 10$ and is well separated from the bound vibrational states. The simulation box is big enough that no wave packet hits numerical boundaries. At the end of simulations, we smoothly filter out the wave packets $R < 10$ and Fourier transform the remaining part into momentum representation, obtaining dissociative wave packets $\tilde{\chi}_g(p_R)$, $\tilde{\chi}_u(p_R)$, and the KER spectrum $P_{g/u}(\mathrm{KER}) = |\tilde{\chi}_{g/u}|^2 M/p_R$ for a single proton. For the given laser parameters, we have tested that the ionization is negligible using the model in Ref. [20], and the total dissociation probability given by the model in Ref. [20] is very similar to those obtained in the current two-channel model. Therefore, the two-channel model can precisely describe the dissociation under the given laser parameters in this section.

B. Simulation results

The dissociation processes that happened in this UV-pump–IR-probe system are depicted in Fig. 1. The attosecond UV pulse resonantly excites H_2^+ from $1s\sigma_g$ to $2p\sigma_u$, generating a dissociating wave packet. The time-delayed IR pulse guides the following dissociation channels: (1) The wave packet directly dissociates through $2p\sigma_u$ (channel 1, abbreviated as $C1_u$). (2) The molecule emits one photon and is dumped to $1s\sigma_g$, then dissociates along $1s\sigma_g(C2_g)$. (3) The molecule is dumped to $1s\sigma_g$ by emitting three IR photons, then is pumped to $2p\sigma_u$ by absorbing one IR photon, and finally dissociates through $2p\sigma_u$ ($C3_u$). (4) The molecule emits three IR photons and dissociates through $1s\sigma_g$ ($C4_g$, not shown in Fig. 1). The one- and three-photon interactions mainly occur when $R = 4.75$ and 3.28 a.u., where the energy gaps between $1s\sigma_g$ and $2p\sigma_u$ are equal to $\omega_{\rm IR}$ and $3\omega_{\rm IR}$, respectively. Physically it is possible to absorb five or even seven photons with much smaller probabilities. Laser intensities and pulse durations decide the dissociation probabilities along these several dissociation channels.

We scan IR intensities and calculate KER. Figure 2 displays (a) $|\tilde{\chi}_g(I,\mathrm{KER})|^2$, (b) $|\tilde{\chi}_u(I,\mathrm{KER})|^2$, (c) $|\tilde{\chi}_l(I,\mathrm{KER})|^2$, and (d) $|\tilde{\chi}_r(I,\mathrm{KER})|^2$, where $\tilde{\chi}_{l/r} = (\tilde{\chi}_g \pm \tilde{\chi}_u)/\sqrt{2}$. Note that the bound vibrational states have been filtered out. Figures 2(a) and 2(b) clearly show different dissociation behaviors when different IR intensities are applied. As depicted in Fig. 1, the UV pulse resonantly excites H_2^+ to $2p\sigma_u$. When the IR intensity is very weak (around 10^{10} W/cm^2), the molecule mainly directly dissociates along $2p\sigma_u$ ($C1_u$), with little probability to interact with the IR field during its dissociation. The KER is simply converted from the molecular potential. In this case, the electron distributes on two nuclei equally. With the increasing of the laser intensity ($10^{12} \sim 10^{13}$ W/cm^2), more and more populations on $2p\sigma_u$ are transferred to $1s\sigma_g$. When the IR intensity is about $10^{12.5}$ W/cm^2, the dissociation probabilities along $C1_u$ and $C2_g$ are almost equal, and the superposition of these two channels makes the electron almost locate all on the right nucleus, as shown in Figs. 2(c) and 2(d). When the intensity is $10^{13} \sim 6\times10^{13}$ W/cm^2, χ_u is very likely dumped to χ_g, i.e., $C2_g$ is the dominant dissociation channel. The further increase of the IR intensity ($10^{13.8} \sim 10^{14}$ W/cm^2) opens $C3_u$. The superposition of $C2_g$ and $C3_u$ makes the

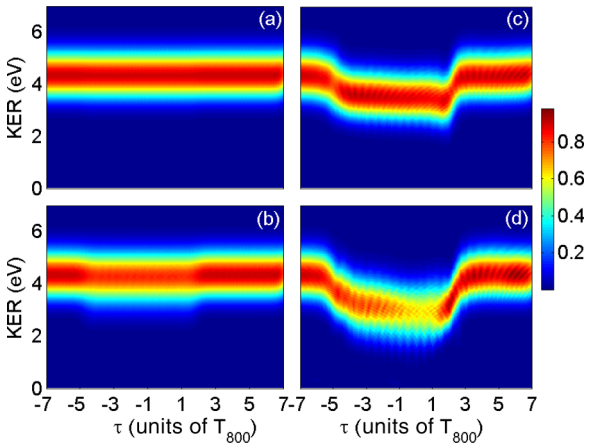

FIG. 3. (Color online) Delay-dependent KER when the IR intensities are (a) 10^{10}, (b) 10^{12}, (c) $10^{13.5}$, and (d) 10^{14} W/cm^2. The carrier envelope phase is $\theta = 0$.

electron locate on the left nucleus with larger probabilities when the IR intensity is about 10^{14} W/cm^2.

In the above analysis, the net three-photon channel $C4_g$ is absent. To open this channel, two factors have to be satisfied. First, the laser intensity must be strong enough to induce three-photon emission. Second, when the internuclear distance increases to 4.75 a.u., the laser intensity must be weak enough to avoid the one-photon absorption process. Therefore, to realize the net three-photon emission process, the IR laser pulse should be strong and short enough. McKenna *et al.* have experimentally demonstrated that the short enough laser pulse is necessary to observe a net three-photon process [42].

The KER as a function of time delay is shown in Fig. 3 when laser intensities are (a) 10^{10}, (b) 10^{12}, (c) $10^{13.5}$, and (d) 10^{14} W/cm^2. In these panels, the KER is constant when the time delay is out of the range $[-5T_{800}, 3T_{800}]$, in which the KER is purely transformed from the molecular potential and the IR field has nearly no influence on the dissociation. On the contrary, when $-5T_{800} < \tau < 3T_{800}$, the KER shows different characters. For the very weak IR field ($\sim 10^{10}$ W/cm^2), the KER does not change. When the laser intensity is about 10^{12} W/cm^2, $C1_u$ and $C2_g$ coexist, therefore, the KER spectrum is broadened. When the intensity is $10^{13.5}$ W/cm^2, $C1_u$ is almost depleted, and $C2_g$ is dominant, therefore, the KER is lowered about half an IR-photon energy. Once the intensity is as high as 10^{14} W/cm^2, $C2_g$ and $C3_u$ coexist, therefore, the KER is further lowered and broadened.

Figure 4(a) shows the dependence of electron localization on UV-IR time delays and IR intensities. The asymmetry parameter is defined as $A = \int(|\tilde{\chi}_l|^2 - |\tilde{\chi}_r|^2)\,d\mathrm{KER} / \int(|\tilde{\chi}_l|^2 + |\tilde{\chi}_r|^2)\,d\mathrm{KER}$. For delays $\tau < 0$, the UV pulse precedes the IR pulse. When delays vary in $[-4T_{800}, T_{800}]$, the IR field with a constant intensity acts on the dissociating H_2^+, consequently, the asymmetry parameter oscillates periodically with the time delay. On the contrary, the asymmetry parameter deviates from the periodical oscillation when the time delay is around $-5T_{800}$ or $2T_{800}$, which is due to the fact that the laser fields of the turn-on or the turn-off parts have different intensities. With increasing laser intensities, the stripes for asymmetry parameters tilt rightward. Along

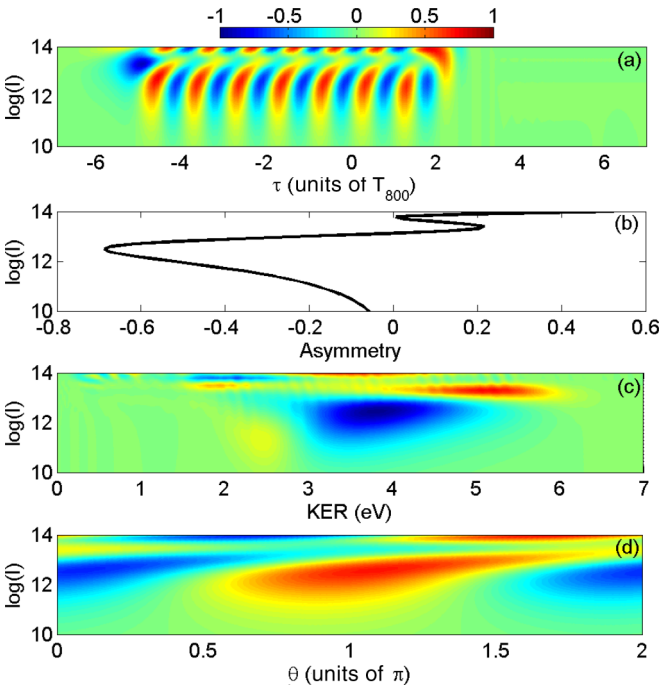

FIG. 4. (Color online) (a) Left-right asymmetry parameters as a function of the time delay τ and the IR intensity when $\theta = 0$. (b) Left-right asymmetry as a function of IR intensities at the time delay $\tau = -1.2T_{800}$. This is taken from (a). (c) KER-dependent asymmetry at the time delay $\tau = -1.2T_{800}$. (d) Left-right asymmetry parameters as a function of the carrier envelope phase and the IR intensity when the time delay is fixed at $\tau = -1.2T_{800}$. The base of the logarithm in the whole paper is 10.

each stripe, the asymmetry parameters change signs when the IR intensity is around $10^{13.6}$ W/cm^2. For a fixed time delay (for example, $\tau = -1.2T_{800}$), the asymmetry parameters may be positive or negative, as shown in Fig. 4(b), meaning that the expected electron moving directions can follow or oppose the laser electric force, which has already been explored in [20] based on the conception of "momentum gate." Here, we decompose the left-right asymmetry into the KER-dependent left-right asymmetry, as shown in Fig. 4(c). One may see that asymmetry parameters depend on KER sensitively. Figure 4(d) shows the dependence of the asymmetry on KER and the carrier envelope phase of the IR field.

The electron asymmetric localization may be understood either in a classical picture or in a quantal picture. In the classical picture, during the molecular dissociation, the interatomic barrier is higher and higher with increasing internuclear distance. When the internuclear distance is about 6.3 a.u., the interatomic barrier blocks the electron movement between two nuclei and the electron localization is frozen. Therefore, the final electron localization depends on the laser steering direction just before the internuclear distance becomes 6.3 a.u. However, for different nuclear energies, the internuclear distances reach 6.3 a.u. within a different time, which means the electron will see different instantaneous laser fields when the internuclear distance is 6.3 a.u. and be steered to different nuclei. This is the fundamental reason that the electron asymmetric localization depends on nuclear energies. When the molecule dissociates along $C1_u$, $C2_g$, or $C3_u$, the nuclear

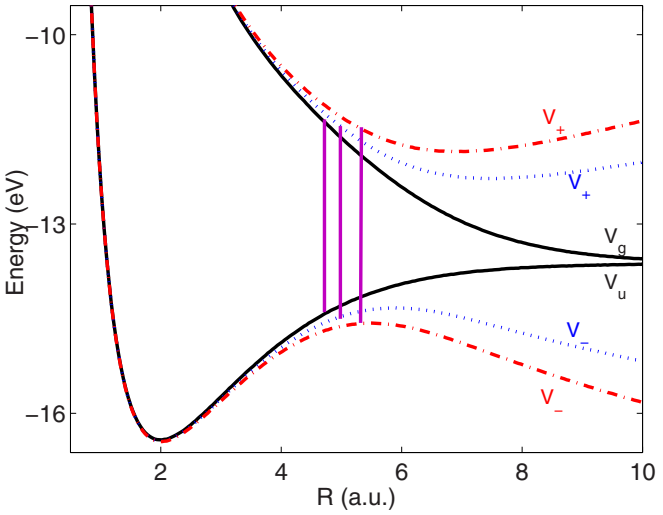

FIG. 5. (Color online) The field-dressed potential curves when the instantaneous laser intensities are 0 (black solid curves), 5×10^{12} W/cm^2 (blue dotted curves), and 10^{13} W/cm^2 (red dash-dotted curves). The three solid vertical curves indicate the internuclear distances where 400-nm pulse induced resonant transitions between V_- and V_+ happen.

energies are different, therefore, the electron asymmetries are also different. In a quantal picture, the asymmetry is due to the interference of different dissociation channels with opposite parities. When the laser intensity is intermediate, the main dissociation channels are $C1_u$ (ungerade) and $C2_g$ (gerade). The left-right asymmetry depends on the relative phase between $C1_u$ and $C2_g$. When the laser intensity is as high as 10^{14} W/cm^2, the main dissociation channels are $C2_g$ (gerade) and $C3_u$ (ungerade). Different dissociation channels induce different interferences, resulting in different electron asymmetries. The relative phase, which depends on laser intensities and time delays and carrier envelope phases, will decide which nucleus has a larger probability to attract the

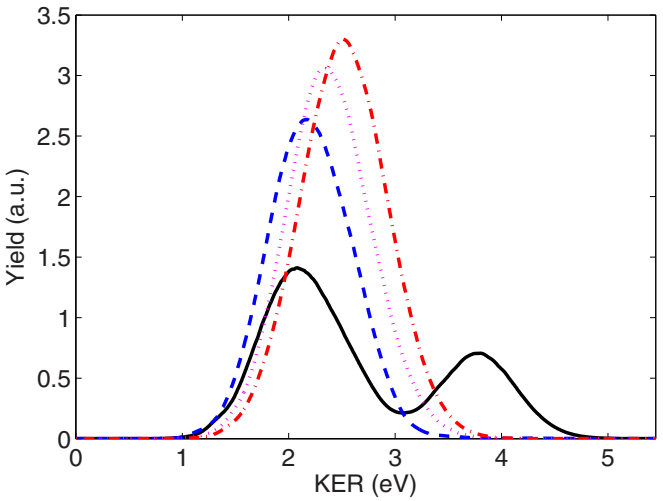

FIG. 6. (Color online) The KER spectra when the 10 000-nm laser pulse has the intensity 0 (black solid curve), 10^{12} W/cm^2 (blue dashed curve), 5×10^{12} W/cm^2 (magenta dotted curve), and 10^{13} W/cm^2 (red dash-dotted curve). The 400-nm laser intensity is fixed at 10^{13} W/cm^2.

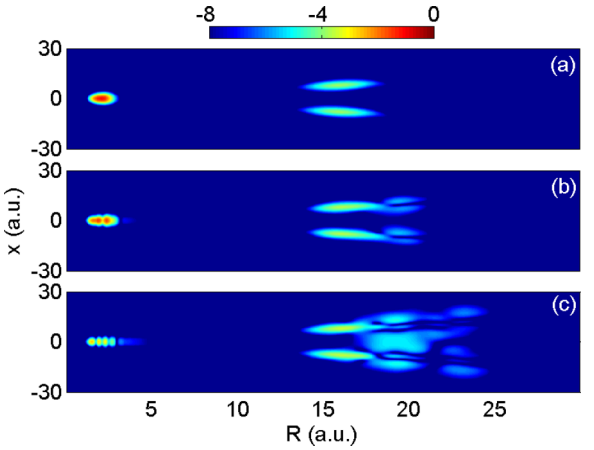

FIG. 7. (Color online) Wave-packet distribution in logarithmic scale as the UV intensities are (a) 10^{13}, (b) 10^{14}, and (c) 10^{15} W/cm^2.

electron. The KER-resolved asymmetry is complementary to the conception of "momentum gate" in Wigner representation [20], in which KER information has been integrated. Since different laser intensities will result in different asymmetries, it is very important to count on the focal volume average [44], as done in [16,17].

III. DISSOCIATION DRESSED BY A FAR-INFRARED LASER PULSE

In this section, we study the Stark effect on the dissociation of H_2^+ with the same numerical model as that in Sec. II. Three laser pulses are used during the whole dissociation. The UV pulse triggers the dissociation along $2p\sigma_u$, and a time-delayed 400-nm laser pulse makes the transition between $1s\sigma_g$ and $2p\sigma_u$. Different from before, this transition is dressed by a laser pulse with a wavelength of 10 000 nm. The combined three-laser pulse is written as

$$E = E_{\mathrm{UV}} \cos[\omega_{\mathrm{UV}}(t+\tau)] \exp\{-2\ln 2[(t+\tau)/\tau_{\mathrm{UV}}]^2\} + E_{10000} \cos(\omega_{10000} t + \theta) \exp[-2\ln 2(t/\tau_{10000})^2] + E_{400} \cos(\omega_{400} t) \exp[-2\ln 2(t/\tau_{400})^2]. \quad (4)$$

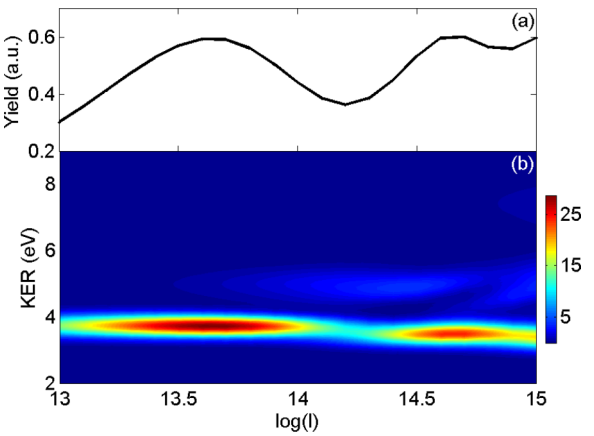

FIG. 8. (Color online) (a) Dissociation probability and (b) KER spectrum as a function of the UV intensity. The base of the logarithm in the whole paper is 10.

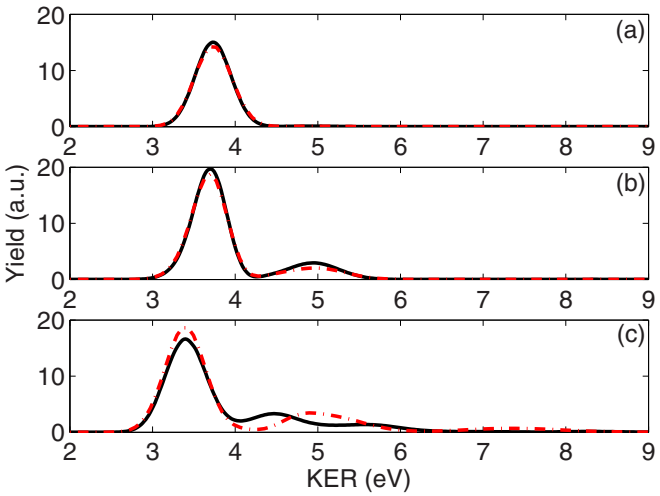

FIG. 9. (Color online) The KER spectra calculated with the eight-channel numerical model (black solid line) and the two dimensional model [Eq. (6)] (red dashed line) when the UV intensities are (a) 10^{13}, (b) 10^{14}, and (c) 10^{15} W/cm^2.

Three laser pulses have the durations τ_{10000}, τ_{400}, $\tau_{\rm UV}$ of their own two optical cycles. The UV and 400-nm pulse intensities are both 10^{13} W/cm^2. The time delay τ is fixed at 270 a.u., and $\theta = 0.15\pi$. We choose such τ and θ because within τ the UV-triggered dissociative wave packet propagates to the internuclear distance around 4∼5 a.u., where the energy gap between $1s\sigma_g$ and $2p\sigma_u$ is close to the photon energy of the 400-nm laser field, and the instantaneous far-infrared laser electric field is maximum. Hence, the 400-nm laser pulse will almost make a resonant transition between $1s\sigma_g$ and $2p\sigma_u$ dressed by a maximum instantaneous electric field.

Because of the Stark shift caused by the 10 000-nm laser field, the two potential curves $1s\sigma_g$ and $2p\sigma_u$ degenerate at large internuclear distances. The laser-modified potential curves become

$$V_\pm = \frac{V_g(R)+V_u(R)}{2} \pm\sqrt{\frac{[V_g(R)-V_u(R)]^2}{4}+[E(t)V_{gu}(R)]^2}. \quad (5)$$

Figure 5 shows the $V_\pm$ when the instantaneous intensities are 0, 5×10^{12}, and 10^{13} W/cm^2. For a stronger dressed laser intensity, the 400-nm induced resonant transition happens in a larger internuclear distance, as marked by the three vertical solid lines. Therefore, for a stronger 10 000-nm pulse, the nuclear wave packet propagates along V_+ more before it is dumped down to V_- by the 400-nm laser pulse, which results in the KER shift, as shown in Fig. 6. In the case of no 10 000-nm pulse, two peaks in the spectrum appear. This is because the 400-nm pulse dumps partly dissociating wave packets on V_+ (or $2p\sigma_u$) to V_- (or $1s\sigma_g$), and the two peaks correspond to the dissociation along V_+ and V_-, respectively. The dependence of KER on the carrier envelope phase of THz pulse has been explained in Ref. [43].

IV. ABSORPTION OF HIGH ENERGETIC PHOTONS

When H_2^+ is exposed to a strong UV field, it may absorb several UV photons and be excited to higher electronic states. Thus, H_2^+ may dissociate along selected potential curves, gaining different KERs. This kind of experiment may be potentially carried on the recently developed free-electron laser instruments [45] in leading laboratories.

A. Numerical model

Though higher potential energy curves are far from $1s\sigma_g$ and $2p\sigma_u$, H_2^+ may still be transferred to high electronic states by absorbing a few high-energy photons. In this case, instead of solving Eq. (2), we simulate the following two-dimensional TDSE:

$$i\frac{\partial}{\partial t}\Psi(x,R;t) = \left[-\frac{1}{M}\frac{\partial^2}{\partial R^2}-\frac{1}{2}\frac{\partial^2}{\partial x^2}+V(x,R,t)\right]\Psi(x,R;t), \quad (6)$$

with the potential

$$V(x,R,t) = \frac{1}{R}-\frac{1}{\sqrt{(x-R/2)^2+s(R)}} -\frac{1}{\sqrt{(x+R/2)^2+s(R)}}+xE(t). \quad (7)$$

The laser electric field is written as $E(t) = E_0\cos(\omega t)\exp[-2\ln 2(t/\tau)^2]$ with τ being four optical cycles. We choose the R-dependent soft core $s(R)$ [46] in order to obtain the precise $1s\sigma_g$ potential curve. After the laser field is finished, we keep propagating the wave packet until the nuclear momentum is converged. R and x span areas [0,30] and [−30,30] a.u., respectively. The spatial steps $\Delta x = 0.2$ a.u., $\Delta R = 0.04$ a.u., and the time step $\Delta t = 0.05$ a.u. Please note that the time step here is much smaller than the time step used in Secs. II and III. This is because here we need a very small time step to resolve the ultrafast movement of the electron. Whereas in Secs. II and III only the nuclear wave function is propagated. The simulation box is big enough that no dissociative wave packets reach its boundaries; however, the ionization is absorbed by the boundaries [47]. The photon energy of the attosecond pulse is $\omega = 0.37$ a.u., matching the energy gap between $1s\sigma_g$ and $2p\sigma_u$ at the equilibrium internuclear distance. Note that the potential curves are obtained by imaginarily propagating

TABLE I. Dissociation probabilities along different electronic states.

State	1	2	3	4	5	6	7	8
Population (10^{13} W/cm^2)	10^{-8}	3×10^{-1}	2×10^{-3}	4×10^{-10}	7×10^{-6}	7×10^{-7}	3×10^{-10}	7×10^{-7}
Population (10^{14} W/cm^2)	10^{-6}	3.7×10^{-1}	8×10^{-2}	3×10^{-7}	10^{-3}	4×10^{-4}	3×10^{-5}	5×10^{-4}
Population (10^{15} W/cm^2)	2×10^{-3}	3.8×10^{-1}	9×10^{-2}	5×10^{-5}	2×10^{-3}	4×10^{-3}	3×10^{-2}	4×10^{-3}

Eq. (6) under fixed internuclear distances, and these potential curves are a little bit different from those in Secs. II and III.

B. Simulation results

We show the snapshots of wave-function distribution in Fig. 7 when UV intensities are (a) 10^{13}, (b) 10^{14}, and (c) 10^{15} W/cm^2. In this section, the pulse duration $\tau = 1.6$ fs, corresponding to four optical periods. When the UV intensity is as low as 10^{13} W/cm^2, the dissociation wave packet has the maximum distribution on the lines $x = \pm R/2$ and has no nodal structure around nuclei along the x axis, indicating the electron is on the atomic $1s$ state. By projecting the dissociative wave packet onto molecular states, we have found the proportion of $2p\sigma_u$ is as large as 99%. When the UV intensity is 10^{14} W/cm^2, the dissociation wave packet may be divided into two parts. Besides the part on atomic $1s$ state, the headmost dissociative wave packet has a node, illustrating itself in the first excited atomic state. From this, we may conclude that the two-channel model in Secs. II and III is not complete to describe this dissociation. When the UV intensity is 10^{15} W/cm^2, more excited states are involved and the electron distribution shows more complex structures.

Figure 8(a) shows the dissociation probability and Fig. 8(b) the KER spectrum as a function of UV intensities. One may see the dissociation probability does not increase monotonically with the increasing of UV intensities. This can be explained by a Rabi oscillation [43,48]. When the UV intensity is higher than 10^{14} W/cm^2, several peaks in the KER spectrum are clearly observed.

To identify the dissociation pathways, we build an eight-channel model under BOA [48] and compare it with the simulation of Eq. (6). The compared KERs are shown in Figs. 9(a)–9(c), corresponding to UV intensities of 10^{13}, 10^{14}, and 10^{15} W/cm^2, respectively. The two models agree with each other precisely in Figs. 9(a) and 9(b), implying that the eight electronic states are enough to describe the UV-induced transition. However, when the UV intensity is 10^{15} W/cm^2, the KER spectra obtained from the two methods do not overlap in the whole spectra. Nevertheless, the eight-channel model may identify the dissociative pathways for a relatively wide range of UV intensities. Table I shows the dissociative probabilities along the eight potential surfaces for different laser intensities. From Table I, we may identify that the peak in Fig. 9(a) is attributed to the dissociation along the first excited electronic state, and the two peaks in Fig. 9(b) are attributed to the dissociation along the first and second excited electronic states.

The tiny discrepancy of two results based on two simulation models in Fig. 9(a) is originated from the BOA, which is confirmed by comparing the KER spectra obtained from the eight-channel model (black solid line) and non-BOA two-dimensional TDSE (red dashed line) for the dissociation of H_2^+, D_2^+, and T_2^+ in Figs. 10(a)–10(c), respectively, where the inserts are the enlargements of the KER peaks. For heavier nuclei, BOA is more reliable, and the discrepancy of KER spectra is indeed smaller. Comparing the three isotopic molecular ions, T_2^+ has the highest peak value in the KER spectra. This is because the heavier nuclei move slower, hence the nuclear wave packet has a longer time to stay in the internuclear distance where the resonant excitation happens.

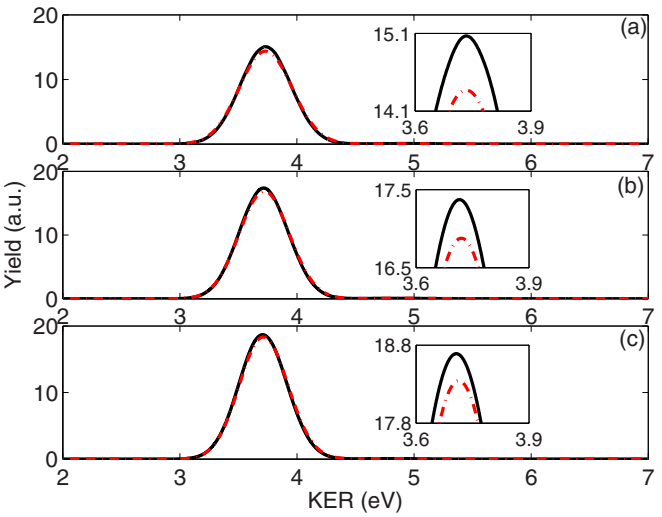

FIG. 10. (Color online) KER spectra for dissociative fragments of (a) H_2^+, (b) D_2^+, and (c) T_2^+. The black solid and red dash-dotted curves are simulation results obtained with the eight-channel model and the two-dimensional model [Eq. (6)], respectively. The spectra peaks are enlarged in the inserts. The UV intensity is 10^{13} W/cm^2.

V. CONCLUSION

In conclusion, we have systematically studied the KER in the dissociation of hydrogen molecular ions in laser fields with different photon energies and intensities. For the 800-nm laser pulse, H_2^+ may dissociate directly, or accompanying one or net two photoemission, ending with different KER. The mixture of different dissociation pathways leads to the asymmetric electron localization on two nuclei. If the dissociation process is dressed by quasistatic fields, the nuclear wave packet will propagate on the Stark-shift potential energy surfaces, resulting in the intensity-dependent KER shift. When the photon energy is large or the laser intensity is very strong, the two-channel model does not work since the molecular ion may be excited to higher electronic states or even ionized. The comparison of the eight-channel model and beyond BOA TDSE simulation may identify dissociation channels and the rationality of the BOA.

ACKNOWLEDGMENTS

This work was supported by NSF of China (Grants No. 11104180, No. 11175120, No. 11121504, No. 11322438), and the Fok Ying-Tong Education Foundation for Young Teachers in the Higher Education Institutions of China (Grant No. 131010).

[1] C. R. Calvert, W. A. Bryan, W. R. Newell, and I. D. Williams, Phys. Rep. **491**, 1 (2010).

[2] A. Giusti-Suzor, F. H. Mies, L. F. DiMauro, E. Charron, and B. Yang, J. Phys. B **28**, 309 (1995).

[3] A. D. Bandrauk and M. L. Sink, J. Chem. Phys. **74**, 1110 (1981).
[4] P. H. Bucksbaum, A. Zavriyev, H. G. Muller, and D. W. Schumacher, Phys. Rev. Lett. **64**, 1883 (1990).
[5] L. J. Frasinski, J. H. Posthumus, J. Plumridge, K. Codling, P. F. Taday, and A. J. Langley, Phys. Rev. Lett. **83**, 3625 (1999).
[6] A. Giusti-Suzor, X. He, O. Atabek, and F. H. Mies, Phys. Rev. Lett. **64**, 515 (1990).
[7] S. Chelkowski, A. D. Bandrauk, and P. B. Corkum, Phys. Rev. Lett. **93**, 083602 (2004).
[8] D. Ray, F. He, S. De, W. Cao, H. Mashiko, P. Ranitovic, K. P. Singh, I. Znakovskaya, U. Thumm, G. G. Paulus, M. F. Kling, I. V. Litvinyuk, and C. L. Cocke, Phys. Rev. Lett. **103**, 223201 (2009).
[9] P. Lan, E. J. Takahashi, and K. Midorikawa, Phys. Rev. A **86**, 013418 (2012).
[10] K. Liu, Q. Zhang, and P. Lu, Phys. Rev. A **86**, 033410 (2012).
[11] V. Roudnev, B. D. Esry, and I. Ben-Itzhak, Phys. Rev. Lett. **93**, 163601 (2004).
[12] M. F. Kling, Ch. Siedschlag, A. J. Verhoef, J. I. Khan, M. Schultze, Th. Uphues, Y. F. Ni, M. Uiberacker, M. Drescher, F. Krausz, and M. J. J. Vrakking, Science **312**, 246 (2006).
[13] X. M. Tong and C. D. Lin, Phys. Rev. Lett. **98**, 123002 (2007).
[14] S. Chatterjee, B. Dutta, and S. S. Bhattacharyya, Phys. Rev. A **83**, 063413 (2011).
[15] I. Znakovskaya, P. von den Hoff, G. Marcus, S. Zherebtsov, B. Bergues, X. Gu, Y. Deng, M. J. J. Vrakking, R. Kienberger, F. Krausz *et al.*, Phys. Rev. Lett. **108**, 063002 (2012).
[16] N. G. Kling, K. J. Betsch, M. Zohrabi, S. Zeng, F. Anis, U. Ablikim, B. Jochim, Z. Wang, M. Kübel, M. F. Kling, K. D. Carnes, B. D. Esry, and I. Ben-Itzhak, Phys. Rev. Lett. **111**, 163004 (2013).
[17] T. Rathje, A. M. Sayler, S. Zeng, P. Wustelt, H. Figger, B. D. Esry, and G. G. Paulus, Phys. Rev. Lett. **111**, 093002 (2013).
[18] G. Sansone, F. Kelkensberg, J. F. Perez-Torres, F. Morales, M. F. Kling, W. Siu, O. Ghafur, P. Johnsson, M. Swoboda, E. Benedetti, F. Ferrari, F. Lepine, J. L. Sanz-Vicario, S. Zherebtsov, I. Znakovskaya, A. L'Huillier, M. Yu. Ivanov, M. Nisoli, F. Martin, and M. J. J. Vrakking, Nature (London) **465**, 763 (2010).
[19] F. He, C. Ruiz, and A. Becker, Phys. Rev. Lett. **99**, 083002 (2007).
[20] F. He, A. Becker, and U. Thumm, Phys. Rev. Lett. **101**, 213002 (2008).
[21] F. He, C. Ruiz, and A. Becker, J. Phys. B: At. Mol. Opt. Phys. **41**, 081003 (2008).
[22] K. P. Singh, F. He, P. Ranitovic, W. Cao, S. De, D. Ray, S. Chen, U. Thumm, A. Becker, M. M. Murnane, H. C. Kapteyn, I. V. Litvinyuk, and C. L. Cocke, Phys. Rev. Lett. **104**, 023001 (2010).
[23] M. Kremer, B. Fischer, B. Feuerstein, V. L. B. de Jesus, V. Sharma, C. Hofrichter, A. Rudenko, U. Thumm, C. D. Schröter, R. Moshammer, and J. Ullrich, Phys. Rev. Lett. **103**, 213003 (2009).
[24] B. Fischer, M. Kremer, T. Pfeifer, B. Feuerstein, V. Sharma, U. Thumm, C. D. Schröter, R. Moshammer, and J. Ullrich, Phys. Rev. Lett. **105**, 223001 (2010).
[25] D. Yang and Shu-Lin Cong, Phys. Rev. A **84**, 013424 (2011).
[26] F. Anis and B. D. Esry, Phys. Rev. Lett. **109**, 133001 (2012).
[27] J. Wu, M. Magrakvelidze, L. P. H. Schmidt, M. Kunitski, T. Pfeifer, M. Schöffler, M. Pitzer, M. Richter, S. Voss, H. Sann, H. Kim, J. Lower, T. Jahnke, A. Czasch, U. Thumm, and R. Dörner, Nat. Commun. **4**, 2177 (2013).
[28] F. He, Phys. Rev. A **86**, 063415 (2012).
[29] A. Fischer, A. Sperl, P. Cörlin, M. Schönwald, H. Rietz, A. Palacios, A. Gonzalez-Castrillo, Fernando Martin, T. Pfeifer, J. Ullrich, A. Senftleben, and R. Moshammer, Phys. Rev. Lett. **110**, 213002 (2013).
[30] A. Staudte, D. Pavičić, S. Chelkowski, D. Zeidler, M. Meckel, H. Niikura, M. Schöffler, S. Schössler *et al.*, Phys. Rev. Lett. **98**, 073003 (2007).
[31] F. He and A. Becker, J. Phys. B: At. Mol. Opt. Phys. **41**, 074017 (2008).
[32] Z. T. Liu, K. J. Yuan, C. C. Shu, W. H. Hu, and S. L. Cong, J. Phys. B: At. Mol. Opt. Phys. **43**, 055601 (2010).
[33] A. Picón, A. Jaroń-Becker, and A. Becker, Phys. Rev. Lett. **109**, 163002 (2012).
[34] A. Kiess, D. Pavičić, T. W. Hänsch, and H. Figger, Phys. Rev. A **77**, 053401 (2008).
[35] R. Bhattacharya and S. S. Bhattacharyya, Phys. Rev. A **79**, 043415 (2009).
[36] J. J. Hua and B. D. Esry, Phys. Rev. A **80**, 013413 (2009).
[37] J. McKenna, A. M. Sayler, B. Gaire, N. G. Johnson, E. Parke, K. D. Carnes, B. D. Esry, and I. Ben-Itzhak, Phys. Rev. A **80**, 023421 (2009).
[38] J. McKenna, F. Anis, A. M. Sayler, B. Gaire, N. G. Johnson, E. Parke, K. D. Carnes, B. D. Esry, and I. Ben-Itzhak, Phys. Rev. A **85**, 023405 (2012).
[39] E. P. Benis, M. Bakarezos, N. A. Papadogiannis, M. Tatarakis, S. Divanis, C. ÓBroin, and L. A. A. Nikolopoulos, Phys. Rev. A **86**, 043428 (2012).
[40] Eric Charron, Annick GiustiSuzor, and Frederick H. Meis, J. Chem. Phys. **103**, 7359 (1995).
[41] M. D. Feit, J. A. Fleck, Jr., and A. Steiger, J. Comput. Phys. **47**, 412 (1982).
[42] J. McKenna, A. M. Sayler, F. Anis, B. Gaire, Nora G. Johnson, E. Parke, J. J. Hua, H. Mashiko, C. M. Nakamura, E. Moon, Z. Chang, K. D. Carnes, B. D. Esry, and I. Ben-Itzhak, Phys. Rev. Lett. **100**, 133001 (2008).
[43] T. Y. Xu and F. He, Phys. Rev. A **88**, 043426 (2013).
[44] A. S. Alnaser, X. M. Tong, T. Osipov, S. Voss, C. M. Maharjan, B. Shan, Z. Chang, and C. L. Cocke, Phys. Rev. A **70**, 023413 (2004).
[45] E. Hemsing, G. Stupakov, D. Xiang, and A. Zholents, Rev. Mod. Phys. **86**, 897 (2014).
[46] K. C. Kulander, F. H. Mies, and K. J. Schafer, Phys. Rev. A **53**, 2562 (1996).
[47] F. He, C. Ruiz, and A. Becker, Phys. Rev. A **75**, 053407 (2007).
[48] X. Y. You and F. He, Phys. Rev. A **89**, 063405 (2014).